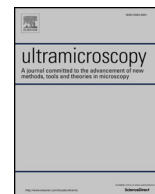




ELSEVIER

Contents lists available at ScienceDirect

Ultramicroscopy

journal homepage: www.elsevier.com/locate/ultramic

Effect of cation ratio and order on magnetic circular dichroism in the double perovskite $\text{Sr}_2\text{Fe}_{1+x}\text{Re}_{1-x}\text{O}_6$

Ping-Luen Ho^a, Chu-Ping Yu^{a,b}, Qiqi Zhang^a, Kyung Song^c, James P. Buban^d, Si-Young Choi^d, Rafal E. Dunin-Borkowski^e, Joachim Mayer^{e,f}, Nyan-Hwa Tai^b, Jing Zhu^a, Lei Jin^{e,*}, Xiaoyan Zhong^{a,*}

^a National Center for Electron Microscopy in Beijing, Key Laboratory of Advanced Materials (MOE), The State Key Laboratory of New Ceramics and Fine Processing, School of Materials Science and Engineering, Tsinghua University, Beijing 100084, China

^b Department of Materials Science and Engineering, National Tsing-Hua University, Hsinchu 30013, Taiwan

^c Materials Modeling and Characterization Department, Korea Institute of Materials Science, Changwon 642-831, South Korea

^d Department of Materials Science and Engineering, Pohang University of Science and Technology, Pohang 37673, South Korea

^e Ernst Ruska-Centre for Microscopy and Spectroscopy with Electrons, Forschungszentrum Jülich GmbH, 52425 Jülich, Germany

^f Central Facility for Electron Microscopy, RWTH Aachen University, 52074 Aachen, Germany

ARTICLE INFO

Keywords:

Electron energy-loss magnetic chiral dichroism

Double perovskite

$\text{Sr}_2\text{FeReO}_6$

Cation ratio

Cation disorder

ABSTRACT

Superexchange-based magnetic coupling of the two B-site cations in rock-salt-ordered double perovskite oxides is extremely sensitive to the cation ratio and degree of order. However, as a result of the limited spatial resolution of most magnetic characterization techniques, it is challenging to establish a direct relationship between magnetic properties and structure in these materials, including the effects of elemental segregation and cation disorder. Here, we use electron energy-loss magnetic chiral dichroism together with aberration-corrected electron microscopy and spectroscopy to record magnetic circular dichroism (MCD) spectra at the nm scale, in combination with structural and chemical information at the atomic scale from the very same region. We study nanoscale phases in ordered $\text{Sr}_2[\text{Fe}][\text{Re}]\text{O}_6$, ordered $\text{Sr}_2[\text{Fe}][\text{Fe}_{1/5}\text{Re}_{4/5}]\text{O}_6$ and disordered $\text{Sr}[\text{Fe}_{4/5}\text{Re}_{1/5}]\text{O}_3$ individually, in order to understand the role of cation ratio and order on local magnetic coupling. When compared with ordered $\text{Sr}_2[\text{Fe}][\text{Re}]\text{O}_6$, we find that antiferromagnetic $\text{Fe}^{3+}\text{-O}^{2-}\text{-Fe}^{3+}$ superexchange interactions arising from an excess of Fe suppress the MCD signal from Fe cations in ordered $\text{Sr}_2[\text{Fe}][\text{Fe}_{1/5}\text{Re}_{4/5}]\text{O}_6$, while dominant $\text{Fe}^{3+}\text{-O}^{2-}\text{-Fe}^{3+}$ antiferromagnetic coupling in disordered $\text{Sr}[\text{Fe}_{4/5}\text{Re}_{1/5}]\text{O}_3$ leads to a decrease in MCD signal down to the noise level. Our work demonstrates a protocol that can be used to correlate crystallographic, electronic and magnetic information in materials such as $\text{Sr}_2\text{Fe}_{1+x}\text{Re}_{1-x}\text{O}_6$, in order to provide insight into structure-property relationships in double perovskite oxides at the atomic scale.

1. Introduction

Double perovskite oxides with the formula $\text{A}_2\text{BB}'\text{O}_6$ (e.g., A = Sr, Ca or Ba; B = Fe or Cr; B' = Re, Mo or W) have attracted considerable attention, owing to their metallic conductivity and ferrimagnetic properties, with Curie temperatures that are significantly higher than those of any manganite and potential applications in magneto-electronic devices [1–3]. Two crystallographically-equivalent six-fold-coordinated sites, B_1 and B_2 [4], can be occupied by individual B or B' species or a combination of B and B' in certain ratios. They can alternate in three-dimensional checkerboard patterns, ideally forming a rock-salt-ordered $\text{A}_2[\text{B}]_{B_1}[\text{B}']_{B_2}\text{O}_6$ structure [5]. As a result of chemical flexibility at the B_1 and B_2 sites, the complexity of $\text{A}_2\text{BB}'\text{O}_6$, including the

possibility of B-site cation disorder and/or partial substitution, can lead to different magnetic ground states and electronic band structures [2,6], which can in turn influence material properties and device functionality. For example, the double perovskite $\text{Sr}_2[\text{Fe}]_{B_1}[\text{Re}]_{B_2}\text{O}_6$ has a half-metallic ferrimagnetic ground state with a large tunnelling magnetoresistance at room temperature (RT) [1,7,8], whereas $\text{Sr}_2[\text{Fe}]_{B_1}[\text{Fe}_{1/3}\text{Re}_{2/3}]_{B_2}\text{O}_6$ is a ferrimagnetic semiconductor [8].

Standard magnetic characterization techniques, such as neutron diffraction [9–11], X-ray magnetic circular dichroism (XMCD) [12,13], Mössbauer spectroscopy [8,14], superconducting quantum interference device (SQUID) magnetometry [11,14] and vibrating sample magnetometry (VSM) [15,16], have been applied for decades in an attempt to obtain a full understanding of the effects of cation ratio and/or order on

* Corresponding author.

E-mail addresses: ljin@fz-juelich.de (L. Jin), xyzhong@mail.tsinghua.edu.cn (X.Y. Zhong).

<https://doi.org/10.1016/j.ultramic.2018.06.009>

Received 11 February 2018; Received in revised form 10 May 2018; Accepted 10 June 2018
Available online 14 June 2018

0304-3991/ © 2018 Elsevier B.V. All rights reserved.

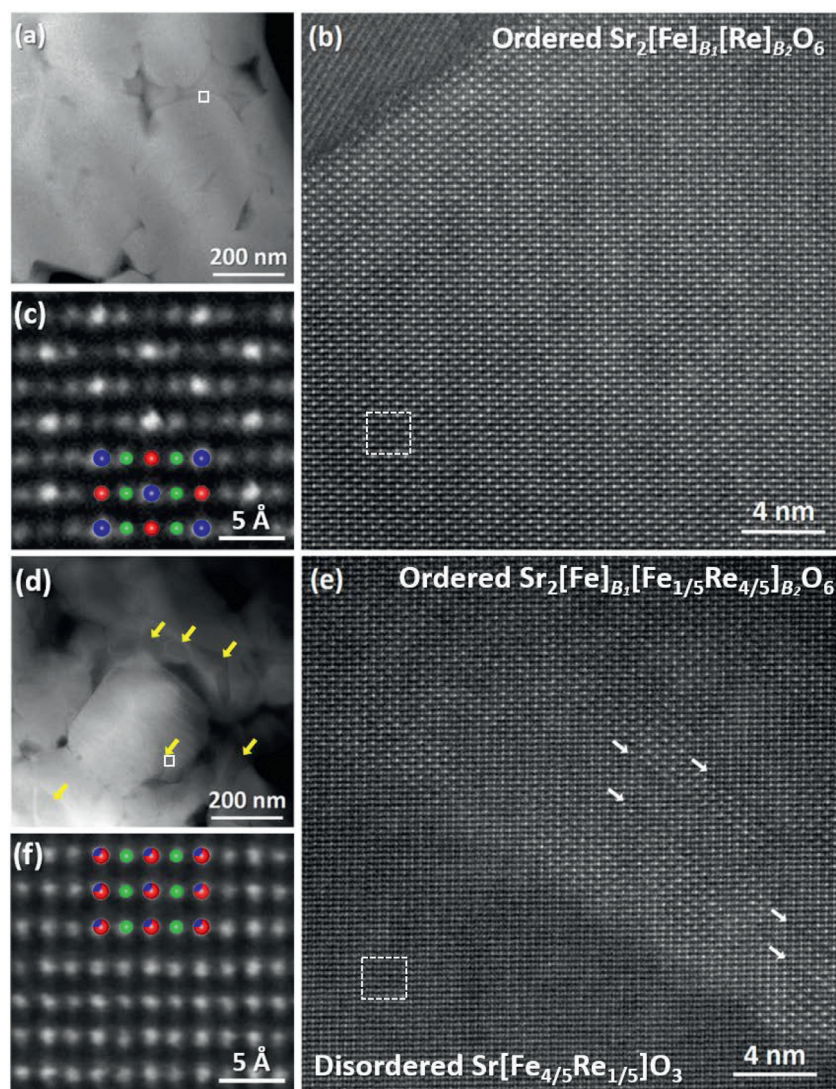


Fig. 1. Regions (b) and (e) correspond to the white solid squares marked in (a) and (d), respectively. Regions (c) and (f) correspond to the white dashed squares marked in (b) and (e), respectively. The atomic-resolution images were recorded along $\langle 011 \rangle_{pc}$ and reveal intensity modulations at *B*-sites in grains that exhibit bright contrast in (a) and (c). Antiphase boundaries in ordered $\text{Sr}_2[\text{Fe}]_{B_1}[\text{Fe}_{1/5}\text{Re}_{4/5}]_{B_2}\text{O}_6$, which are marked by white arrows in (e), are identified based on atomic positions in antiphase domains that display a crystal translation. Grains with lower intensity in (d) are marked by yellow arrows and correspond to the absence of *B*-site order in $\text{Sr}[\text{Fe}_{4/5}\text{Re}_{1/5}]\text{O}_3$ in (e, f). Atomic models superimposed on (c) and (f) show Sr in green, Re in blue, Fe in red and mixed Re and Fe in blue and red. (For interpretation of the references to colour in this figure legend, the reader is referred to the web version of this article.)

the magnetic behaviour of $\text{Sr}_2\text{Fe}_{1+x}\text{Re}_{1-x}\text{O}_6$. Abe et al. used Mössbauer absorption spectroscopy to determine cation arrangements in $\text{Sr}_2\text{FeReO}_6$ and $\text{Sr}_2\text{Fe}_{4/3}\text{Re}_{2/3}\text{O}_6$ to be $\text{Sr}_2[\text{Fe}^{3+}]_{B_1}[\text{Re}^{5+}]_{B_2}\text{O}_6$ and $\text{Sr}_2[\text{Fe}^{3+}]_{B_1}[\text{Fe}_{1/3}^{3+}\text{Re}_{2/3}^{6+}]_{B_2}\text{O}_6$, respectively [8]. Incomplete magnetic saturation in $\text{Sr}_2\text{Fe}_{4/3}\text{Re}_{2/3}\text{O}_6$ measured using VSM was thought to result from structural imperfections, such as *B*-site cation disorder, whereas complete saturation of magnetization was achieved easily in $\text{Sr}_2\text{FeReO}_6$. The RT magnetization of $\text{Sr}_2\text{FeReO}_6$ was found to be approximately twice that of $\text{Sr}_2\text{Fe}_{4/3}\text{Re}_{2/3}\text{O}_6$ and $\text{Sr}_2\text{Fe}_{11/9}\text{Re}_{7/9}\text{O}_6$ in an applied field of 7.5 kOe. Pannunzio Miner et al. used synchrotron X-ray powder diffraction to determine Fe/Re occupancies in $\text{Sr}_2\text{Fe}_{4/3}\text{Re}_{2/3}\text{O}_6$ of $\text{Sr}_2[\text{Fe}_{0.57}\text{Re}_{0.43}]_{B_1}[\text{Fe}_{0.76}\text{Re}_{0.24}]_{B_2}\text{O}_6$ [17]. X-ray diffraction (XRD), neutron powder diffraction and SQUID measurements have also been combined to show that $\text{Sr}_2\text{FeReO}_6$ with 75% Fe/Re cation order has a saturation magnetization of $1.1 \mu_B/\text{mol}$, whereas $\text{Sr}_2\text{FeReO}_6$ with complete Fe/Re cation order has a saturation magnetization of $2.58 \mu_B/\text{mol}$ [11]. Choi et al. used high-angle annular dark-field scanning transmission electron microscopy (HAADF-STEM) to image atomic structures in materials with different types of cation disorder, including

antisite defects, antiphase boundaries and disordered Re-deficient phases distributed in pristine SFRO and Re-excess SFRO at the nm scale [18]. The relatively low saturation magnetization of pristine SFRO measured using VSM was attributed to the presence of such defective structures [16]. However, as a result of the inability to record spatially-resolved high-resolution magnetic information using conventional magnetic characterization techniques, these reports failed to verify the influence of local defective structures on magnetic properties directly.

Electron energy-loss magnetic chiral dichroism (EMCD) can be used to record magnetic circular dichroism (MCD) with high spatial resolution as a result of the short wavelength of high-energy transmitted electrons [19–23]. The EMCD technique was first proposed in 2003 [24], demonstrated experimentally in 2006 [19] and developed rapidly in recent years [25–29]. In our previous studies, we measured spin and orbital magnetic moments quantitatively on the nm scale, with the spatial resolution determined by the probe size used under convergent beam illumination conditions [30–34]. Here, we record structural, chemical and magnetic information from three nanoscale phases of ordered $\text{Sr}_2[\text{Fe}][\text{Re}]\text{O}_6$, ordered $\text{Sr}_2[\text{Fe}][\text{Fe}_{1/5}\text{Re}_{4/5}]\text{O}_6$ and disordered

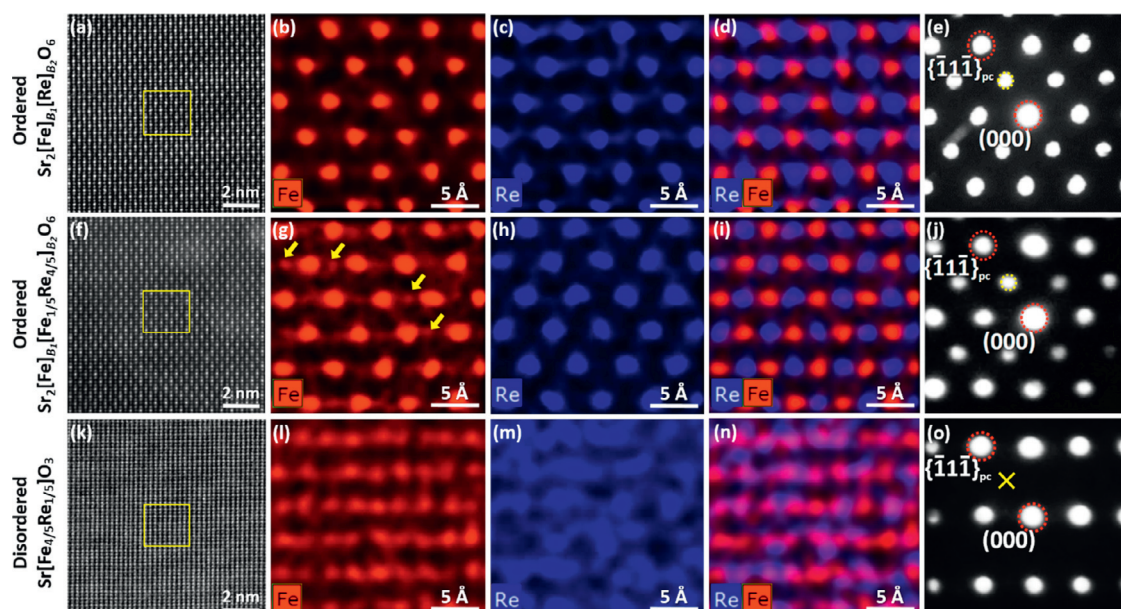


Fig. 2. Atomic-resolution elemental mapping and nanodiffraction of ordered $\text{Sr}_2[\text{Fe}]_{B_1}[\text{Re}]_{B_2}\text{O}_6$, ordered $\text{Sr}_2[\text{Fe}]_{B_1}[\text{Fe}_{1/5}\text{Re}_{4/5}]_{B_2}\text{O}_6$ and disordered $\text{Sr}[\text{Fe}_{4/5}\text{Re}_{1/5}]\text{O}_3$ viewed along $\langle 011 \rangle_{pc}$. HAADF-STEM images, Fe maps (red), Re maps (blue), mixed Fe and Re maps (red and blue) and nanodiffraction patterns are shown in (a–e) for ordered $\text{Sr}_2[\text{Fe}]_{B_1}[\text{Re}]_{B_2}\text{O}_6$, (f–j) for ordered $\text{Sr}_2[\text{Fe}]_{B_1}[\text{Fe}_{1/5}\text{Re}_{4/5}]_{B_2}\text{O}_6$ and (k–o) for disordered $\text{Sr}[\text{Fe}_{4/5}\text{Re}_{1/5}]\text{O}_3$, respectively. (For interpretation of the references to colour in this figure legend, the reader is referred to the web version of this article.)

$\text{Sr}[\text{Fe}_{4/5}\text{Re}_{1/5}]\text{O}_3$ using HAADF-STEM imaging, energy dispersive X-ray (EDX) spectroscopy and EMCD, in order to assess the effects of cation ratio and disorder on local magnetization.

2. Materials and methods

Two polycrystalline $\text{Sr}_2\text{Fe}_{1+x}\text{Re}_{1-x}\text{O}_6$ samples were synthesized using a conventional solid state method, which is described elsewhere [16]. Briefly, a sample denoted SFRO-0Re was prepared with a nominal stoichiometric ratio of SrCO_3 , Fe_2O_3 , and ReO_3 , while another sample with 15 mol% Re excess, denoted SFRO-15Re, was prepared in order to compensate for the volatility of Re. Specimens for transmission electron microscopy (TEM) were prepared using mechanical grinding, dimpling and polishing. Final Ar ion milling was carried out on a Bal-Tec Res-101 system.

Atomic-resolution HAADF-STEM imaging was performed at 300 kV using an FEI Themis 60–300 microscope equipped with a double spherical aberration corrector with a STEM resolution of 60 pm. EDX elemental mapping was carried out at 200 kV on an FEI 80–200 probe-corrected ChemiSTEM microscope equipped with a high brightness field emission gun and a Super-X EDS system, comprising four SDD detectors, with a STEM spatial resolution of 80 pm [35]. The datasets were acquired for 10 to 30 minutes with at least 1024×768 pixels and processed using Bruker Esprit software. Statistical analysis of cation compositions was obtained from elemental maps recorded over regions of several tens of nm in size for arbitrary grain orientations. Electron energy-loss spectroscopy (EELS) and EMCD experiments under parallel beam illumination conditions were performed at 200 kV on an FEI Tecnai F20 microscope equipped with a Gatan Tridiem spectrometer using an energy resolution of approximately 1.2 eV, a beam diameter of approximately 100 nm and an EELS semi-collection angle of approximately 2.5 mrad. Nanodiffraction, EELS and EMCD experiments under nanobeam illumination conditions were performed at 300 kV on an FEI Titan 80–300 microscope equipped with a Gatan Tridiem spectrometer using an energy resolution of approximately 0.8 eV [36], a beam size of approximately 2 nm and semi-convergence and semi-collection angles of approximately 0.84 and 1.91 mrad, respectively. Optimized diffraction conditions and aperture positions were identified using dynamical

diffraction calculations [27]. Two- and three-beam conditions in EMCD experiments were achieved based on Kikuchi lines and diffraction pattern intensities. Data processing of EEL spectra included pre-edge background subtraction, removal of plural scattering by Fourier-ratio deconvolution and normalization by integration of the post-edge intensity [37]. Sample thicknesses were determined from low-loss EEL spectra.

3. Structural and chemical characterization of $\text{Sr}_2\text{Fe}_{1+x}\text{Re}_{1-x}\text{O}_6$

Fig. 1 shows HAADF-STEM images recorded from (a–c) SFRO-15Re and (d–f) SFRO-0Re. Over a large field of view, the image of SFRO-15Re in Fig. 1a has almost the same intensity, while the image of SFRO-0Re in Fig. 1d shows local regions of lower intensity, as indicated by yellow arrows. The bright and dark stripes visible in the central grain in Fig. 1d arise from spatial interference between the scanning grid of the electron beam and the atomic lattice of the specimen [38]. Our statistical EDX measurements of cation composition indicate that grains in SFRO-15Re have an Fe:Re ratio of 0.52:0.48 (standard deviation $\sigma = 0.01$), while bright and dark regions in SFRO-0Re have Fe:Re ratios of 0.60:0.40 ($\sigma = 0.02$) and 0.81:0.19 ($\sigma = 0.05$), respectively. For simplicity, we denote these regions as $\text{Sr}_2\text{FeReO}_6$, $\text{Sr}_2\text{Fe}_{6/5}\text{Re}_{4/5}\text{O}_6$ and $\text{Sr}_2\text{Fe}_{8/5}\text{Re}_{2/5}\text{O}_6$, respectively. They are further denoted $\text{Sr}_2[\text{Fe}]_{B_1}[\text{Re}]_{B_2}\text{O}_6$, $\text{Sr}_2[\text{Fe}]_{B_1}[\text{Fe}_{1/5}\text{Re}_{4/5}]_{B_2}\text{O}_6$ and $\text{Sr}[\text{Fe}_{4/5}\text{Re}_{1/5}]\text{O}_3$, respectively, after confirming the cation occupancy. Further discussions are presented below.

Fig. 1b and Fig. 1c show atomic-resolution HAADF-STEM images of a $\text{Sr}_2[\text{Fe}]_{B_1}[\text{Re}]_{B_2}\text{O}_6$ grain recorded along $\langle 011 \rangle_{pc}$. Close examination of the enlarged HAADF-STEM image in Fig. 1c reveals the atomic arrangements. Atomic columns of SrO (green), Fe (red) and Re (blue) can be distinguished from each other based on column intensity differences (Z-contrast), confirming rock-salt-type order of Fe and Re on the B_1 and B_2 sites of the double perovskite lattice. Similar order can be observed in the $\text{Sr}_2[\text{Fe}]_{B_1}[\text{Fe}_{1/5}\text{Re}_{4/5}]_{B_2}\text{O}_6$ phases in the SFRO-0Re sample, as shown in Fig. 1e. Such B-site order is not present in the Re-deficient phases (marked by yellow arrows in Fig. 1d), as revealed in the higher-magnification HAADF image in Fig. 1f. It is also apparent that many antiphase domain boundaries, as indicated by white arrows, are present

in the $\text{Sr}_2[\text{Fe}]_{B_1}[\text{Fe}_{1/5}\text{Re}_{4/5}]_{B_2}\text{O}_6$ phases.

Fe/Re cation order on the atomic scale was investigated by using EDX elemental mapping of the $\text{Fe } K_{\alpha}$ signal at 6.405 keV and the $\text{Re } K_{\alpha}$ signal at 8.652 keV, in addition to recording nanodiffraction patterns along $\langle 011 \rangle_{pc}$, from three square regions of ordered $\text{Sr}_2[\text{Fe}]_{B_1}[\text{Re}]_{B_2}\text{O}_6$, ordered $\text{Sr}_2[\text{Fe}]_{B_1}[\text{Fe}_{1/5}\text{Re}_{4/5}]_{B_2}\text{O}_6$ and disordered $\text{Sr}[\text{Fe}_{4/5}\text{Re}_{1/5}]\text{O}_3$, as shown in Fig. 2 (a, f, k). Three HAADF-STEM images in Fig. 2(a, f, k) show single-crystalline regions of the three phases without any defects or boundaries and were selected for structural, chemical and magnetic characterization. The composite color maps show that Fe (red) and Re (blue) stack alternately at B -sites in both $\text{Sr}_2[\text{Fe}]_{B_1}[\text{Re}]_{B_2}\text{O}_6$ (Fig. 2d) and $\text{Sr}_2[\text{Fe}]_{B_1}[\text{Fe}_{1/5}\text{Re}_{4/5}]_{B_2}\text{O}_6$ (Fig. 2i), while they are distributed more randomly in $\text{Sr}[\text{Fe}_{4/5}\text{Re}_{1/5}]\text{O}_3$ (Fig. 2n). Such features are consistent with the Z -contrast images shown in Fig. 1 and Fig. 2(a, f, k). They give rise to half-integer spots, e.g., $1/2[\bar{1}\bar{1}\bar{1}]_{pc}$, super-reflection spots, which are marked by dotted circles in both ordered phases in Fig. 2(e, j), as well as to the extinction of such spots, as marked by a cross in the disordered phase in Fig. 2o. Quantification of the overall EDX spectra yields Fe/Re ratios of approximately 0.51:0.49, 0.58:0.42 and 0.83:0.17 for the three regions of the individual phases. These values are very close to our statistical measurements.

Close examination of the individual maps allows the cation ratios in the ordered phases to be estimated. In the ordered phase shown in Fig. 2f, the atomic-scale Fe map in Fig. 2g indicates that most of the Fe atoms are located on B_1 sites, while a small proportion of the Fe atoms are located on B_2 sites, as indicated by yellow arrows. The atomic-scale Re map shown in Fig. 2h reveals that, within the present detection limit, Re atoms occupy only B_2 sites. In this way, based on the cation occupancy determined from atomic-scale EDX elemental mapping, we identify this $\text{Sr}_2\text{Fe}_{6/5}\text{Re}_{4/5}\text{O}_6$ phase as $\text{Sr}_2[\text{Fe}]_{B_1}[\text{Fe}_{1/5}\text{Re}_{4/5}]_{B_2}\text{O}_6$. Similarly, the $\text{Sr}_2\text{FeReO}_6$ phase (Fig. 2a) and the $\text{Sr}_2\text{Fe}_{8/5}\text{Re}_{2/5}\text{O}_6$ phase (Fig. 2k) are inferred to be $\text{Sr}_2[\text{Fe}]_{B_1}[\text{Re}]_{B_2}\text{O}_6$ and $\text{Sr}[\text{Fe}_{4/5}\text{Re}_{1/5}]\text{O}_3$, respectively.

4. Magnetic and valence state characterization of $\text{Sr}_2\text{Fe}_{1+x}\text{Re}_{1-x}\text{O}_6$

Fig. 3 shows normalized (a-c) Fe EMCD spectra and (d) EEL spectra recorded from a region of ordered $\text{Sr}_2[\text{Fe}]_{B_1}[\text{Re}]_{B_2}\text{O}_6$ with a thickness of 0.27 λ , a region of ordered $\text{Sr}_2[\text{Fe}]_{B_1}[\text{Fe}_{1/5}\text{Re}_{4/5}]_{B_2}\text{O}_6$ with a thickness of 0.29 λ and a region of disordered $\text{Sr}[\text{Fe}_{4/5}\text{Re}_{1/5}]\text{O}_3$ with a thickness of 0.26 λ at RT, where λ is the inelastic electron mean free path. The three phases are the same as those shown in Fig. 2. The experimental EEL spectra S_+ and S_- , which are marked “+” (black) and “-” (red), were recorded at the positive and negative Thales positions, respectively. The aperture positions and corresponding diffraction conditions, with $\{\bar{1}\bar{1}\bar{1}\}_{pc}$ systematic reflections excited, optimized by the theoretical dynamical diffraction calculations, are shown in the insets to Fig. 3(a-c). $1/2[\bar{1}\bar{1}\bar{1}]_{pc}$ super-reflection diffraction spots are visible in both ordered phases, as indicated by yellow dashed circles in Fig. 3(a,b). Since a relatively large illuminated area can be selected for the $\text{Sr}_2[\text{Fe}]_{B_1}[\text{Re}]_{B_2}\text{O}_6$ phase in the SFRO-15Re sample without significant phase separation or elemental segregation, EEL spectra were recorded from this phase using parallel illumination with a beam diameter of approximately 100 nm. Since the ordered $\text{Sr}_2[\text{Fe}]_{B_1}[\text{Fe}_{1/5}\text{Re}_{4/5}]_{B_2}\text{O}_6$ (Fig. 3b) and disordered $\text{Sr}[\text{Fe}_{4/5}\text{Re}_{1/5}]\text{O}_3$ (Fig. 3c) phases are mixed on the nm scale in the SFRO-0Re sample, a convergent nanobeam with a probe size of approximately 2 nm was used for EELS and EMCD acquisition from a relatively small sample area of each phase. As a consequence, the signal to noise ratios in the EMCD spectra acquired from $\text{Sr}_2[\text{Fe}]_{B_1}[\text{Re}]_{B_2}\text{O}_6$ are better than those from the $\text{Sr}_2[\text{Fe}]_{B_1}[\text{Fe}_{1/5}\text{Re}_{4/5}]_{B_2}\text{O}_6$ and $\text{Sr}[\text{Fe}_{4/5}\text{Re}_{1/5}]\text{O}_3$ phases, due to the different illumination conditions.

After normalization by the non-magnetic isotropic ($S_+ + S_-$) spectra, the relative Fe EMCD signals for $\text{Sr}_2[\text{Fe}]_{B_1}[\text{Fe}_{1/5}\text{Re}_{4/5}]_{B_2}\text{O}_6$ are slightly weaker than those for $\text{Sr}_2[\text{Fe}]_{B_1}[\text{Re}]_{B_2}\text{O}_6$, whereas the Fe EMCD signals for disordered $\text{Sr}[\text{Fe}_{4/5}\text{Re}_{1/5}]\text{O}_3$ are close to the noise level. The

near-edge fine structures in the normalized EEL spectra acquired from the three phases are shown in Fig. 3d and are almost identical, confirming the similar trivalent states of the Fe cations. To a large extent, this observation rules out the possibility of significant contributions from oxygen non-stoichiometry in both samples. The valence states of Re cations in $\text{Sr}_2[\text{Fe}]_{B_1}[\text{Fe}_{1/5}\text{Re}_{4/5}]_{B_2}\text{O}_6$ and $\text{Sr}[\text{Fe}_{4/5}\text{Re}_{1/5}]\text{O}_3$ are inferred to increase with increasing Fe/Re ratio, due to the lack of a change in the Fe^{3+} valence states. According to the sum rules [21,37], the orbital to spin magnetic moment ratios (m_L/m_S) obtained from the EMCD spectra for $\text{Sr}_2[\text{Fe}]_{B_1}[\text{Re}]_{B_2}\text{O}_6$ and $\text{Sr}_2[\text{Fe}]_{B_1}[\text{Fe}_{1/5}\text{Re}_{4/5}]_{B_2}\text{O}_6$ are 0.01 ± 0.01 and 0.02 ± 0.01 , respectively, indicating that the orbital magnetic moments of the Fe^{3+} cations are quenched in both ordered phases.

5. Discussion

In ordered $\text{Sr}_2[\text{Fe}]_{B_1}[\text{Re}]_{B_2}\text{O}_6$, only $\text{Fe}^{3+}-\text{O}^{2-}-\text{Re}^{5+}$ superexchange interactions in the rock-salt cation superstructure, without significant $\text{Fe}^{3+}-\text{O}^{2-}-\text{Fe}^{3+}$ superexchange interactions, result in collinear $\text{Sr}_2[\text{Fe}^{3+}(\bar{5}\mu_B)]_{B_1}[\text{Re}^{5+}(\bar{2}\mu_B)]_{B_2}\text{O}_6$ ferrimagnetic configurations, with the B_1 and B_2 sublattices occupied by Fe^{3+} and Re^{5+} , respectively. Although an average antisite defect concentration of approximately 10.5% was inferred from Powder X-ray Diffraction (XRD) patterns recorded from the entire SFRO-15Re sample in previous work [16], the presence of completely ordered $\text{Sr}_2[\text{Fe}]_{B_1}[\text{Re}]_{B_2}\text{O}_6$ regions can be confirmed by using analytical STEM, enabling us to exclude all effects of cation disorder and an inhomogeneous elemental distribution. In this way, intrinsic MCD spectra can be recorded from completely ordered $\text{Sr}_2[\text{Fe}]_{B_1}[\text{Re}]_{B_2}\text{O}_6$ with an Fe/Re ratio of approximately 1:1.

In ordered $\text{Sr}_2[\text{Fe}]_{B_1}[\text{Fe}_{1/5}\text{Re}_{4/5}]_{B_2}\text{O}_6$, the substitution of Fe for Re on B_2 sites resulting from the presence of excess Fe leads to not only $\text{Fe}^{3+}-\text{O}^{2-}-\text{Re}^{5+}$ superexchange interactions, but also $\text{Fe}^{3+}-\text{O}^{2-}-\text{Fe}^{3+}$ and $\text{Fe}^{3+}-\text{O}^{2-}-\text{Re}^{6+}$ superexchange interactions. As a result of the presence of antiferromagnetic $\text{Fe}^{3+}-\text{O}^{2-}-\text{Fe}^{3+}$ superexchange bonds in ferrimagnetic configurations of $\text{Sr}_2[\text{Fe}^{3+}(\bar{5}\mu_B)]_{B_1}[\text{Fe}_{1/5}^{3+}(\bar{5}\mu_B)\text{Re}_{2/5}^{5+}(\bar{2}\mu_B)\text{Re}_{2/5}^{6+}(\bar{1}\mu_B)]_{B_2}\text{O}_6$, a slightly weaker EMCD strength at RT (Fig. 3b) arises from a small proportion of Fe^{3+} magnetic moments cancelling each other out. It was reported in Ref. [8] that incomplete saturation and an approximately 50% decrease in RT magnetization observed in bulk ordered $\text{Sr}_2[\text{Fe}]_{B_1}[\text{Fe}_{1/9}\text{Re}_{8/9}]_{B_2}\text{O}_6$ or $\text{Sr}_2[\text{Fe}]_{B_1}[\text{Fe}_{2/9}\text{Re}_{7/9}]_{B_2}\text{O}_6$ using VSM might be influenced partially by B -site cation disorder, in comparison with the bulk ordered $\text{Sr}_2[\text{Fe}]_{B_1}[\text{Re}]_{B_2}\text{O}_6$ phase. Phase impurity could be another reason and requires detailed investigation. However, this possibility was not mentioned in Ref. [8]. In our case, the decrease in RT magnetization in ordered $\text{Sr}_2[\text{Fe}]_{B_1}[\text{Fe}_{1/5}\text{Re}_{4/5}]_{B_2}\text{O}_6$ determined from the relative EMCD strength is less significant than that measured in similar bulk materials in the work mentioned above, possibly as a result of the exclusion of B -site cation disorder and phase impurity.

In disordered $\text{Sr}[\text{Fe}_{4/5}\text{Re}_{1/5}]\text{O}_3$ with experimentally-determined Fe cation trivalent states, dominant $\text{Fe}^{3+}-\text{O}^{2-}-\text{Fe}^{3+}$ antiferromagnetic coupling leads to mostly cancelled Fe^{3+} magnetic moments, resulting in a marginal EMCD signal at RT (Fig. 3c). In previous work [16], a decrease of approximately 75% in the macroscopic RT magnetization of the SFRO-0Re sample containing ordered $\text{Sr}_2[\text{Fe}]_{B_1}[\text{Fe}_{1/5}\text{Re}_{4/5}]_{B_2}\text{O}_6$ and disordered $\text{Sr}[\text{Fe}_{4/5}\text{Re}_{1/5}]\text{O}_3$ was measured using SQUID magnetometry in a field of approximately 2 T, in comparison with the SFRO-15Re sample containing ordered $\text{Sr}_2[\text{Fe}]_{B_1}[\text{Re}]_{B_2}\text{O}_6$. Such a dramatic decrease in macroscopic RT magnetization may arise from the presence of both disordered $\text{Sr}[\text{Fe}_{4/5}\text{Re}_{1/5}]\text{O}_3$, whose EMCD strength is significantly suppressed, and ordered $\text{Sr}_2[\text{Fe}]_{B_1}[\text{Fe}_{1/5}\text{Re}_{4/5}]_{B_2}\text{O}_6$, whose EMCD strength is partially suppressed.

6. Conclusions

Local measurements of magnetic circular dichroism, atomic

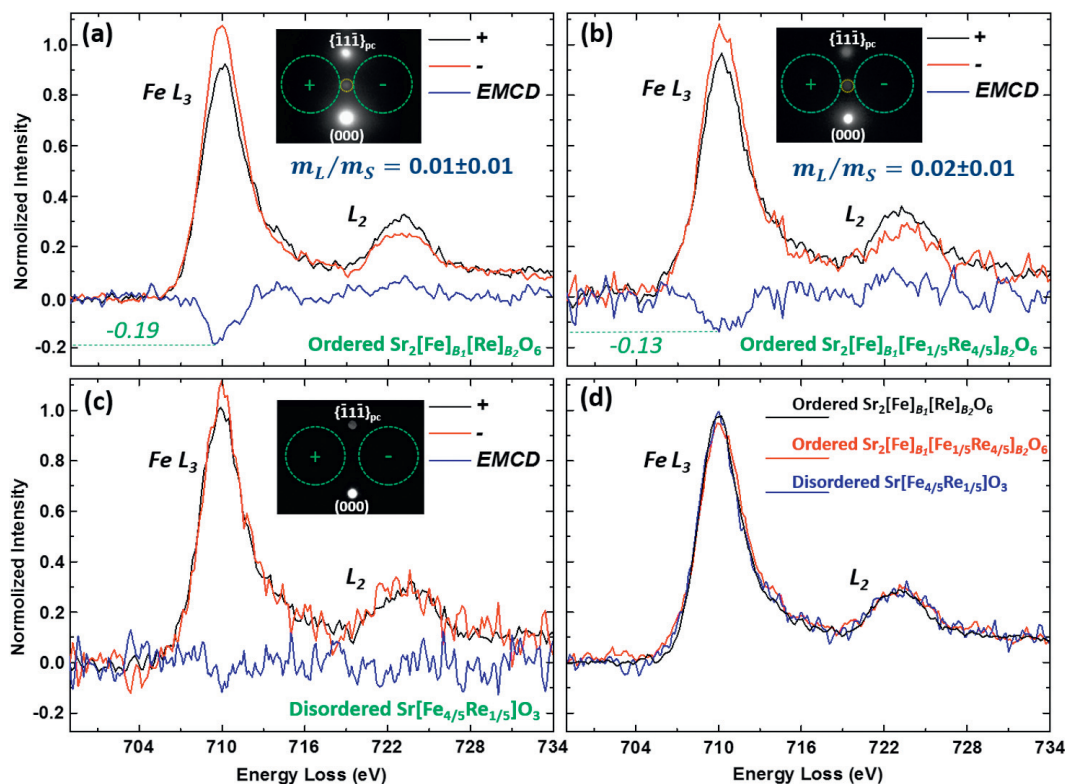


Fig. 3. EMCD spectra of Fe cations in (a) ordered $\text{Sr}_2[\text{Fe}]_{\text{B}_1}[\text{Re}]_{\text{B}_2}\text{O}_6$, (b) ordered $\text{Sr}_2[\text{Fe}]_{\text{B}_1}[\text{Fe}_{1/5}\text{Re}_{4/5}]_{\text{B}_2}\text{O}_6$ and (c) disordered $\text{Sr}[\text{Fe}_{4/5}\text{Re}_{1/5}]\text{O}_3$, shown alongside (d) corresponding electron energy-loss near edge structures. Black and red lines correspond to normalized experimental electron energy-loss spectra recorded using positive “+” and negative “-” aperture positions, while blue lines show spectral differences corresponding to EMCD signals. The aperture positions and diffraction patterns, with $\{111\}_{\text{pc}}$ systematic reflections excited, are shown in the insets. The measured orbital to spin magnetic moment ratios m_L/m_S are indicated. (For interpretation of the references to colour in this figure legend, the reader is referred to the web version of this article.)

arrangement, cation order, chemical state and elemental distribution have been obtained experimentally from individual nanoscale phases in ordered $\text{Sr}_2[\text{Fe}]_{\text{B}_1}[\text{Re}]_{\text{B}_2}\text{O}_6$, ordered $\text{Sr}_2[\text{Fe}]_{\text{B}_1}[\text{Fe}_{1/5}\text{Re}_{4/5}]_{\text{B}_2}\text{O}_6$ and disordered $\text{Sr}[\text{Fe}_{4/5}\text{Re}_{1/5}]\text{O}_3$. Antiferromagnetic $\text{Fe}^{3+}-\text{O}^{2-}-\text{Fe}^{3+}$ super-exchange coupling in a ferrimagnetic configuration of ordered $\text{Sr}_2[\text{Fe}^{3+}(\overline{5\mu_{\text{B}}})]_{\text{B}_1}[\text{Fe}_{1/5}^{3+}(\overline{5\mu_{\text{B}}})\text{Re}_{2/5}^{5+}(\overline{2\mu_{\text{B}}})\text{Re}_{2/5}^{6+}(\overline{1\mu_{\text{B}}})]_{\text{B}_2}\text{O}_6$ is shown to result in a weaker EMCD signal, when compared to completely ordered $\text{Sr}_2[\text{Fe}]_{\text{B}_1}[\text{Re}]_{\text{B}_2}\text{O}_6$, while the EMCD signal measured from disordered $\text{Sr}[\text{Fe}_{4/5}\text{Re}_{1/5}]\text{O}_3$ almost vanishes due to the presence of dominant anti-ferromagnetic $\text{Fe}^{3+}-\text{O}^{2-}-\text{Fe}^{3+}$ bonds. Cation substitution and disordered phases are believed to be the primary reasons for a significant weakening in the RT magnetization of pristine SFRO-0Re obtained using macroscopic VSM measurements. Our approach provides an improved understanding of structure-property relationships at the nm scale in double perovskites with different structural complexities.

Acknowledgements

This paper is dedicated to Professor Jing Zhu on the occasion of her 80th birthday. The work was financially supported by the National Key Research and Development Program [2016YFB0700402], the National Natural Science Foundation of China [51761135131, 51671112, 51471096, 51390471, 51527803], the National Basic Research Program of China [2015CB921700, 2015CB654902], the Fund of Key Laboratory of Advanced Materials of Ministry of Education [2018AML12] and an RWTH Aachen University - Tsinghua University Junior Research Fellowship scheme. R. D.-B. is grateful for funding from the European Research Council under the European Union's Seventh Framework Programme [FP7/2007–2013]/ERC grant agreement number 320832. This work made use of the resources of the National Centre for Electron Microscopy in Beijing and the Ernst Ruska-

Centre for Microscopy and Spectroscopy with Electrons in Forschungszentrum Jülich. K. S., J. P. B. and S.-Y. C. acknowledge the support of the Global Frontier Hybrid Interface Materials of the National Research Foundation of Korea funded by the Korean Government [2013M3A6B1078872]. The authors thank D. S. Song, D. Meertens and M. Kruth for valuable contributions to this work.

Supplementary materials

Supplementary material associated with this article can be found, in the online version, at doi:10.1016/j.ultramic.2018.06.009.

References

- [1] K.-I. Kobayashi, T. Kimura, H. Sawada, K. Terakura, Y. Tokura, Room-temperature magnetoresistance in an oxide material with an ordered double-perovskite structure, *Nature* 395 (1998) 677–680.
- [2] D. Serrate, J.M.De. Teresa, M.R. Ibarra, Double perovskites with ferromagnetism above room temperature, *J. Phys.: Condens. Matter* 19 (2007) 02320.
- [3] S. Vasala, M. Karppinen, $\text{A}_2\text{B}'\text{B}''\text{O}_6$ perovskites: a review, *Prog. Solid State Chem.* 43 (2015) 1–36.
- [4] S. Nakamura, K. Oikawa, Precise structure analysis consistent with Mossbauer quadrupole effect: a case of the ordered double perovskites Sr_2FeMO_6 ($M = \text{Mo}$ and Re), *J. Phys. Soc. Jpn.* 72 (12) (2003) 3123–3127.
- [5] J. Longo, R. Ward, Magnetic compounds of hexavalent rhenium with the perovskite-type structure, *J. Am. Chem. Soc.* 83 (13) (1961) 2816–2818.
- [6] J. Gopalakrishnan, A. Chattopadhyay, S.B. Ogale, T. Venkatesan, R.L. Greene, A.J. Millis, K. Ramesha, B. Hannoyer, G. Marest, Metallic and nonmetallic double perovskites: a case study of A_2FeReO_6 ($A = \text{Ca}, \text{Sr}, \text{Ba}$), *Phys. Rev. B* 62 (2000) 9538.
- [7] K.-I. Kobayashi, T. Kimura, Y. Tomioka, H. Sawada, K. Terakura, Y. Tokura, Intergrain tunneling magnetoresistance in polycrystals of the ordered double perovskite $\text{Sr}_2\text{FeReO}_6$, *Phys. Rev. B* 59 (1999) 11159.
- [8] M. Abe, T. Nakagawa, S. Nomura, Magnetic and Mössbauer studies of the ordered perovskites $\text{Sr}_2\text{Fe}_{1-x}\text{Re}_x\text{O}_6$, *J. Phys. Soc. Jpn.* 35 (5) (1973) 1360–1365.
- [9] J.M. De Teresa, D. Serrate, J. Blasco, M.R. Ibarra, L. Morellon, Impact of cation size on magnetic properties of $(\text{AA})_2\text{FeReO}_6$ double perovskites, *Phys. Rev. B* 69 (2004)

- 144401.
- [10] H. Kato, T. Okuda, Y. Okimoto, Y. Tomioka, K. Oikawa, T. Kamiyama, Y. Tokura, Structural and electronic properties of the ordered double perovskites A_2MReO_6 ($A = Sr, Ca$; $M = Mg, Sc, Mn, Fe, Co, Ni, Zn$), *Phys. Rev. B* 69 (2004) 184412.
- [11] M. Retuerto, M.J. Martínez-Lope, M. García-Hernández, J.A. Alonso, Curie temperature enhancement in partially disordered Sr_2FeReO_6 double perovskites, *Mater. Res. Bull.* 44 (2009) 1261–1264.
- [12] M. Sikora, Cz. Kapusta, M. Borowiec, C.J. Oates, V. Prochazka, D. Rybicki, D. Zajac, J.M. De Teresa, C. Marquina, M.R. Ibarra, Evidence of unquenched *Re* orbital magnetic moment in $AA'FeReO_6$ double perovskites, *Appl. Phys. Lett.* 89 (2005) 062509.
- [13] V.N. Antonov, L.V. Bekenov, A. Ernst, Electronic structure and X-ray magnetic circular dichroism in A_2FeReO_6 ($A = Ca, Sr$, and Ba) oxides, *Phys. Rev. B* 94 (2016) 035122.
- [14] T. Hernández, F. Plazaola, J.M. Barandiarán, J.M. Greneche, Cation order in double perovskite oxide, $Sr_2Fe_{1-x}Sc_xReO_6$ ($x = 0.05, 0.1$), *Hyperfine Interact* 161 (2005) 113–122.
- [15] J.B. Lim, S.-Y. Choi, M.-H. Kim, D. Suvorov, J.-H. Jeon, T.-K. Song, W.-J. Kim, Effect of excess *Re* on the magnetic properties of Sr_2FeReO_6 double-perovskite, *Mater. Lett.* 75 (2012) 143–145.
- [16] T.-W. Lim, S.-D. Kim, K.-D. Sung, Y.-M. Rhyim, H. Jeon, J. Yun, K.-H. Kim, K.-M. Song, S. Lee, S.-Y. Chung, M. Choi, S.-Y. Choi, Insights into cationic ordering in *Re*-based double perovskite oxides, *Sci. Rep.* 6 (2016) 19746.
- [17] E.V. Pannunzio Miner, J.M. De Paoli, J.A. Alonso, M. García-Hernández, R.D. Sánchez, R.E. Carbonio, Ferrimagnetic order in the insulating $Sr_3Fe_2ReO_9$ double perovskite, *Physica B* 398 (2007) 397–400.
- [18] S.-Y. Choi, J.B. Lim, Y. Ikuhara, D. Suvorov, J.-H. Jeon, Direct observation of cationic ordering in double perovskite Sr_2FeReO_6 crystals, *Microsc. Microanal.* 19 (S5) (2013) 25–28.
- [19] P. Schattschneider, S. Rubino, C. Hébert, J. Ruzs, J. Kuneš, P. Novák, E. Carlino, M. Fabrizio, G. Panaccione, G. Rossi, Detection of magnetic circular dichroism using a transmission electron microscope, *Nature* 441 (2006) 486–488.
- [20] P. Schattschneider, M. Stöger-Pollach, S. Rubino, M. Sperl, C. Hurm, J. Zweck, J. Ruzs, Detection of magnetic circular dichroism on the two-nanometer scale, *Phys. Rev. B* 78 (2008) 104413.
- [21] J. Salafranca, J. Gazquez, N. Pérez, A. Labart, S.T. Pantelides, S.J. Pennycook, X. Batlle, M. Varela, Surfactant organic molecules restore magnetism in metal-oxide nanoparticle surfaces, *Nano Lett* 12 (2012) 2499–2503.
- [22] T. Thersleff, J. Ruzs, B. Hjörvarsson, K. Leifer, Detection of magnetic circular dichroism with subnanometer convergent electron beams, *Phys. Rev. B* 94 (2016) 134430.
- [23] J. Ruzs, S. Muto, J. Spiegelberg, R. Adam, K. Tatsumi, D.E. Bügler, P.M. Oppeneer, C.M. Schneider, Magnetic measurements with atomic-plane resolution, *Nat. Commun.* 7 (2016) 12672.
- [24] C. Hébert, P. Schattschneider, A proposal for dichroic experiments in the electron microscope, *Ultramicroscopy* 96 (2003) 463–468.
- [25] J. Ruzs, S. Rubino, P. Schattschneider, First-principles theory of chiral dichroism in electron microscopy applied to 3d ferromagnets, *Phys. Rev. B* 75 (2007) 214425.
- [26] H. Lidbaum, J. Ruzs, A. Liebig, B. Hjörvarsson, P.M. Oppeneer, E. Coronel, O. Eriksson, K. Leifer, Quantitative magnetic information from reciprocal space maps in transmission electron microscopy, *Phys. Rev. Lett.* 102 (2009) 037201.
- [27] J. Ruzs, S. Muto, K. Tatsumi, New algorithm for efficient Bloch-waves calculations of orientation-sensitive ELNES, *Ultramicroscopy* 125 (2013) 81–88.
- [28] Z.C. Wang, A.H. Tavabi, L. Jin, J. Ruzs, D. Tyutyunnikov, H.B. Jiang, Y. Moritomo, J. Mayer, R.E. Dunin-Borkowski, R. Yu, J. Zhu, X.Y. Zhong, Atomic scale imaging of magnetic circular dichroism by achromatic electron microscopy, *Nat. Mater.* 17 (2018) 221–225.
- [29] S. Shunsuke, J. Ruzs, K. Tatsumi, R. Adam, S. Arai, V. Kocovski, P.M. Oppeneer, D.E. Bügler, C.M. Schneider, Quantitative characterization of nanoscale polycrystalline magnets with electron magnetic circular dichroism, *Nat. Commun.* 5 (2014) 3138.
- [30] Z.Q. Wang, X.Y. Zhong, R. Yu, Z.Y. Cheng, J. Zhu, Quantitative experimental determination of site-specific magnetic structures by transmitted electrons, *Nat. Commun.* 4 (2013) 1395.
- [31] D. Song, L. Ma, S. Zhou, J. Zhu, Oxygen deficiency induced deterioration in microstructure and magnetic properties at $Y_3Fe_5O_{12}/Pt$ interface, *Appl. Phys. Lett.* 107 (2015) 042401.
- [32] D. Song, G. Li, J. Cai, J. Zhu, A general way for quantitative magnetic measurement by transmitted electrons, *Sci. Rep.* 6 (2016) 18489.
- [33] Z.C. Wang, X.Y. Zhong, L. Jin, X.F. Chen, Y. Moritomo, J. Mayer, Effects of dynamic diffraction conditions on magnetic parameter determination in a double perovskite Sr_2FeMoO_6 using electron energy-loss magnetic chiral dichroism, *Ultramicroscopy* 176 (2017) 212–217.
- [34] J. Lin, X.Y. Zhong, C. Song, J. Ruzs, V. Kocovski, H.L. Xin, B. Cui, L.L. Han, R.Q. Lin, X.F. Chen, J. Zhu, Detection of magnetic circular dichroism in amorphous materials utilizing a single-crystalline overlayer, *Phys. Rev. Materials* 1 (2017) 071404(R).
- [35] A. Kovács, R. Schierholz, K. Tillmann, FEI Titan G2 80-200 CREWLEY, *J. Large-scale Res. Facil.* 2 (2016) A43.
- [36] M. Heggen, M. Luysberg, K. Tillmann, FEI Titan 80-300 STEM, *J. Large-scale Res. Facil.* 2 (2016) A42.
- [37] J. Ruzs, O. Eriksson, P. Novák, P.M. Oppeneer, Influence of plural scattering on the quantitative determination of spin and orbital moments in electron magnetic chiral dichroism measurements, *Phys. Rev. B* 83 (2011) 132402.
- [38] D. Su, Y. Zhu, Scanning moiré fringe imaging by scanning transmission electron microscopy, *Ultramicroscopy* 110 (2010) 229–233.